

Cite this: *Nanoscale*, 2018, **10**, 15553

On-surface structural and electronic properties of spontaneously formed Tb₂Pc₃ single molecule magnets†

Jack Hellerstedt,[‡] Aleš Cahlík,[‡] Martin Švec,[‡] Bruno de la Torre,^{a,b} María Moro-Lagares,^{a,b} Taras Chutora,^{a,b} Barbora Papoušková,[‡] Giorgio Zoppellaro,[‡] Pingo Mutombo,[‡] Mario Ruben,[‡] Radek Zbořil[‡] and Pavel Jelinek[‡]

The single molecule magnet (SMM) bis(phthalocyaninato)terbium(III) (TbPc₂) has received significant and increasing attention as an exemplar system for realizing molecule-based spin electronics. Attaining higher nuclearity *via* multi-decker TbPc systems has remained an outstanding challenge, as known examples of Tb₂Pc₃ systems are only those containing Pc rings with substituents (*e.g.* alkyl, alkoxy). Here we report on the spontaneous formation of Tb₂Pc₃ species from TbPc₂ precursors *via* sublimation in ultrahigh vacuum (UHV) onto an Ag(111) surface. The presence of Tb₂Pc₃ molecules on the surface are inspected using scanning probe microscopy with submolecular resolution supported by density functional theory (DFT) calculations and additional chemical analysis. We observe the selective presence of a Kondo resonance (30 K) in the Tb₂Pc₃ species, that we attribute to differences in the orientation of the internal molecular ligands. Formation of triple-decker complexes offers new possibilities to study and control magnetic interactions not accessible with standard TbPc₂ molecules.

Received 24th May 2018,
Accepted 29th July 2018

DOI: 10.1039/c8nr04215b

rsc.li/nanoscale

1. Introduction

Single-molecule magnets (SMMs) are metal complexes which act as magnetic domains at the single-molecule level;^{1–3} the nanosize dimensions and quantum nature of SMM systems brings to light several properties that link macroscopic phenomena with the quantum world, such as the emergence of staircase hysteretic behaviour in the magnetisation, quantum phase interference, and temperature independent relaxation processes. SMMs are synthesised by coordinating spin active transition-metal ions (d, f-block) with a variety of organic-based chelating molecules, in such a way that the unpaired electrons located on the metal ions are coupled

together *via* exchange interactions and give rise to systems with high spin multiplicity, and large (as well as negative) zero field splitting with dominant uniaxial magnetic anisotropy.

In particular, the bis(phthalocyaninato) terbium(III) (TbPc₂) molecule, stands out in recent years for being extensively investigated. Structurally, the TbPc₂ molecule adopts a D_{4d} symmetry and a square anti-prismatic terbium coordination geometry. The complex can be synthesised in the anionic form [TbPc₂][−] and in the uncharged (neutral) form [TbPc₂]. These very promising SMM candidates exhibit particularly high energy barriers for magnetisation reversal ($U_{\text{eff}} = 410\text{--}641\text{ cm}^{-1}$ depending on the Pc-ring oxidation states and environment)³ and blocking temperatures ($T_c > 1.7\text{ K}$); properties that are not quenched even when the molecule is subjected to dimensionally constrained environments (*e.g.* following surface deposition).⁴

Further improvements in these properties are expected through increasing the molecule nuclearity by creating a multi-decker TbPc system.^{5,6} It has been previously shown that in pristine Tb₂Pc₃ the dominant interaction of the lanthanide magnetic moments is dipolar in nature, with only a small contribution from exchange.^{5,7} However, the importance to study in more depth the electronic/magnetic properties of Tb₂Pc₃ molecules *vs.* TbPc₂ molecules relies on the fact that the former have two sets of 4f spin active centres that act singly as SMM units,^{5,8} together with the presence of deloca-

^aInstitute of Physics of the Czech Academy of Sciences, v.v.i., Cukrovarnická 10, 162 00 Praha 6, Czech Republic. E-mail: jelinekp@fzu.cz

^bRegional Centre of Advanced Technologies and Materials, Department of Physical Chemistry, Faculty of Science, Palacký University, Šlechtitelů 27, 78371 Olomouc, Czech Republic

^cKarlsruhe Institute of Technology, Institute of Nanotechnology Hermann-von-Helmholtz-Platz 1, 76344 Eggenstein-Leopoldshafen, Germany

^dInstitut de Physique et Chimie des Matériaux de Strasbourg (IPCMS), CNRS-Université de Strasbourg, 67034 Strasbourg, France

†Electronic supplementary information (ESI) available. See DOI: 10.1039/c8nr04215b

‡These authors contributed equally to this work.

lised π -electrons on the Pc rings. Such structural and magneto/electronic organisation offers the opportunity for deepening our understanding of basic physical principles, namely how the coupling between lanthanide cations is susceptible to alteration following molecular interaction with magnetic and/or non-magnetic substrates.

These efforts have been hampered by the insolubility of unsubstituted phthalocyanine rings. Only a few multi-decker lanthanide complexes are known today in literature, and mostly comprise of species making use of substituted Pc-rings (*e.g.* with OEt, OBU, alkyl, alkoxy chains) to increase solubility.³ It has been previously suggested that at elevated temperatures, TbPc₂ molecules may decompose and form Tb₂Pc₃ and Tb₃Pc₄ under certain conditions.⁹ However, solid proof of the existence of Tb₂Pc₃ has been missing so far.

Even in their present state, these key features may promote the technological implementation of the system in real-world devices.^{10–36} In particular, measurements utilizing radio-frequency and magnetic field excitations in TbPc₂ point towards the potential use of this molecule for reading the nuclear spin state information of the Tb atom through the coupled electronic states of the metal ion and the ligands.^{21,37–39}

One prevalent and widely studied phenomena on TbPc₂ molecules is the selective and controllable presence of a zero-bias Kondo resonance in the dI/dV spectra, localized to the Pc ligand lobes.^{11,24,29,31,35,40} The location and strength of the Kondo resonance has been attributed to charge transfer between the substrate and the TbPc₂ molecules.^{10–12,16,18–20,22–25,27,29–31,33–35,40,41} The Kondo phenomenon is observed in all studies conducted on the monolayer TbPc₂ on Au(111)^{24,32} but not on the Ag(111) substrate.²⁹ Nevertheless, in the case of the higher apparent height (*i.e.* brighter) molecules, on Au(111) the Kondo effect is quenched, but is present on Ag(111). In Ara *et al.* in particular, the brighter molecules are considered as a second layer of TbPc₂ molecules.²⁹ Additionally, the Kondo state can be quenched by physical rotation of the top Pc ligand,^{11,15} and has also been shown to be influenced by the ligand neighborhood.³⁵ Spin resolved measurements demonstrate the importance of understanding exactly how interaction between the substrate and molecule, *e.g.*, charge transfer, influences the orbital occupancy and resulting electronic properties of the molecules.¹⁴

Here we report measurements of TbPc₂ molecules thermally evaporated in ultrahigh vacuum (UHV) on a single crystal Ag(111) surface and subsequently studied *via* scanning tunneling (STM) and non-contact atomic force microscopies (nc-AFM).⁴² Submolecular spatial AFM resolution achieved with a CO-terminated probe allows us to identify the presence of well ordered, self-assembled islands composed of both TbPc₂ and Tb₂Pc₃ molecules. The unexpected presence of Tb₂Pc₃ molecules is further supported by manipulation experiments and confirmed by chemical analysis of the molecules collected after the UHV experiments. From these observations we can infer an alternating rotational configuration of the triple Pc ligand stack, which can rationalise the appearance of

the Kondo resonance observed on Tb₂Pc₃ molecules. The experimental evidence is supported by total energy density functional theory (DFT) calculations.

2. Results

After deposition of TbPc₂ molecules on the Ag(111) surface held at room temperature (for details see Methods), we observed in STM large areas (>150 × 400 nm) of densely packed molecules surrounded by clean Ag(111), as shown in Fig. 1(a). The molecular layer grows between surface step edges and we clearly observe two different apparent height contrasts within the molecular layer using STM imaging. Detailed inspection of the edge of an island as shown in Fig. 1(b), reveals two distinct molecular contrasts, dark and bright, which correspond to different apparent heights of molecules. Differences in height have been previously observed in STM measurements for TbPc₂ absorbed on Au(111) and Ag(111) surfaces^{11,29} and additional species with higher apparent height were attributed to a second layer of TbPc₂ molecules.^{29,32}

However, apparent topography measured in STM on the same region may change substantially at different tip-sample biases. Indeed, bias-dependent line profiles, presented in Fig. 2(a), show significant deviation in the apparent STM height between the two different species, making reliable measurement of the height impossible using this method. For certain bias voltages, the higher apparent height molecules are

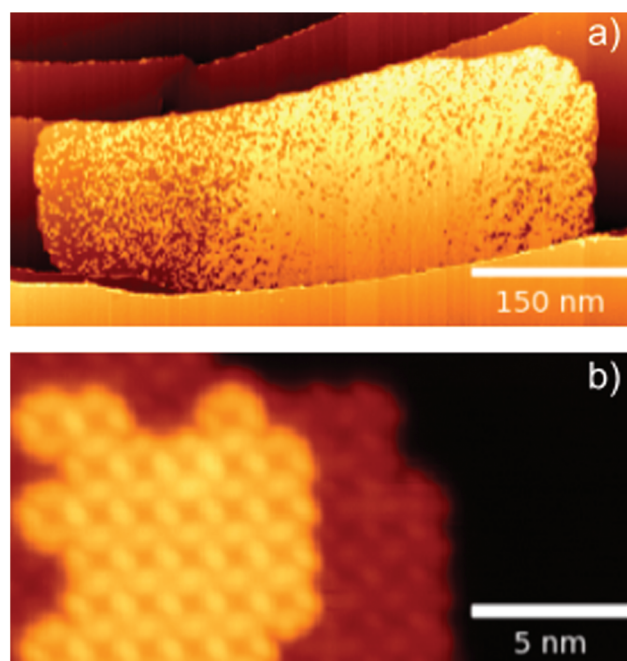


Fig. 1 (a) Overview STM topography ($V_{\text{bias}} = 900$ mV, $I = 10$ pA) showing a close-packed complete molecular island. (b) Close-up STM ($V_{\text{bias}} = 900$ mV, $I = 15$ pA) from island edge showing two heights of molecule and bare Ag(111).

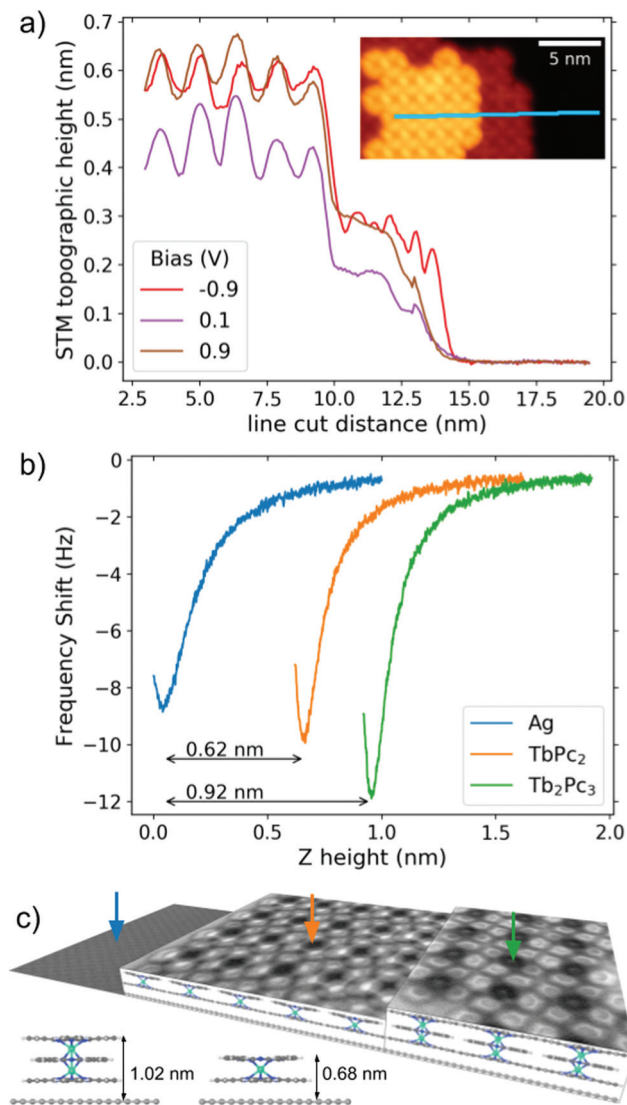


Fig. 2 Comparison of STM and AFM height measurements. (a) Bias-dependent line profiles of inset STM topography ($V_{\text{bias}} = 900$ mV, $I = 15$ pA) showing Tb₂Pc₃, TbPc₂ and bare Ag(111) surface. (b) $\Delta f(z)$ spectroscopies taken on the three different regions indicated by the colored arrows on (c). We use the minima from these curves to determine the heights of TbPc₂ and Tb₂Pc₃ as 0.62 nm and 0.92 nm, respectively. (c) Schematic diagram showing multi-height high-resolution imaging of the Ag(111), TbPc₂ and Tb₂Pc₃ molecules. The DFT optimized models have heights of 0.68 and 1.02 nm, shown in the lower left corner.

roughly double that of the lower apparent height molecules relative to the Ag(111) surface, which is likely why they have previously been identified as a second layer of TbPc₂ molecules.^{29,32}

STM and AFM height determination

To overcome this deficiency in STM height determination, we examined the apparent heights in the nc-AFM mode using a CO-terminated tip. The presence of an inert CO molecule on the metallic tip apex significantly reduces the chemical reactivity of the probe, which allows us to reach the frequency shift

minima without variation of tip structure. This measurement has been previously demonstrated to be an accurate way to determine the heights of molecules absorbed on surfaces.⁴³ The frequency shift was recorded as a function of tip-sample distance on the two different molecular regions and Ag(111) surface, as shown in Fig. 2(b). By identifying the frequency shift minimum on the three regions (dark, bright molecules and bare Ag(111) surface), we obtained the height of the two different molecular regions to be 0.62 nm and 0.92 nm with respect to the Ag(111) surface. Systematic error in these values due to energetic contributions beyond the dominant Pauli repulsion have been previously shown to be on the order of pm, far below the height difference we observe here.^{43,44} In contrast with the apparent height from STM, these measurements show that the higher molecules are not twice as high as their lower counterparts. On the other hand, the two AFM determined heights match well with the distances between the upper Pc ligand of TbPc₂ and Tb₂Pc₃, with respect to the Ag(111) surface as obtained from the total energy DFT simulations, shown in Fig. 2(c). This finding strongly suggests that the higher and lower molecules in STM represent Tb₂Pc₃ and TbPc₂ molecules, respectively.

Molecular manipulation of Tb₂Pc₃

We performed manipulation experiments of the bright molecules, the results of which further reinforce the identification of Tb₂Pc₃ on Ag(111). Fig. 3 shows a sequence of molecular manipulations performed by moving the tip in constant height laterally into the side of different bright molecules, with the direction of tip motion indicated by the arrows. The two tones of bright molecules are likely due to the presence or absence of the Kondo effect discussed later in the manuscript. We expected lateral manipulations to move what we initially supposed to be second layer TbPc₂ molecules. Instead, for the lateral manipulations in Fig. 3(a)–(c), the bright molecule was completely removed from the area (e.g., absorbed to the tip), leaving a hole down to the substrate. The removal of the molecules in Fig. 3(b) and (c) created a channel that was required for the successful lateral movement of the higher molecule, shown in Fig. 3(d). We interpret these observations as evidence that the species with higher apparent height in STM are chemically discrete units, consistent with our identification of them as Tb₂Pc₃.

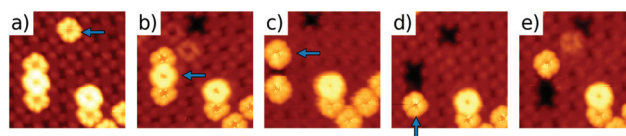


Fig. 3 Manipulation experiments performed on Tb₂Pc₃ molecules, indicated by the blue arrows. (a) Initial state of the region. (b) When extracted (absorbed to the tip), hole down to bare Ag surface becomes visible. (c) and (d) show the removal of additional Tb₂Pc₃ species to create a channel; (d) and (e) demonstrate how the remaining Tb₂Pc₃ moves laterally in the channel as a discrete unit. The surrounding less bright molecules are TbPc₂.

Ex situ chemical analysis

To gain more evidence of the formation of the Tb_2Pc_3 molecules, we performed *ex situ* chemical analysis of the molecules before and after several thermal cycles of evaporation in UHV onto the Ag(111) surface. High-resolution mass spectrometry (time-of-flight tandem mass spectrometer, Q-TOF) for residual material remaining in the crucible after the UHV experiments, confirms the presence of both the TbPc_2 and Tb_2Pc_3 species (ESI,† $[\text{TbPc}_2]^+$ with $1183.2\ m/z^+$ and $[\text{Tb}_2\text{Pc}_3]^+$ with $1855.3\ m/z^+$) as well as the presence of increasing signatures attributable to half-decker Tb molecules $[\text{TbPc}]^+$ (see the ESI, Fig. S6–S11†). From these observations we conclude that thermal decomposition in the UHV chamber appears to promote a temperature-induced structural rearrangement of the TbPc_2 molecules, like what has been shown earlier,⁹ following a reaction pathway tentatively highlighted by the following scheme:



where ΔT and Δt represent the annealing temperature and time, respectively.

To further test the impact of the annealing temperature and time in promoting the structural rearrangement of TbPc_2 molecules, we screened the pristine material after the annealing process at three different temperatures (700 K, 675 K, 650 K) and short annealing time ($t = 10$ min). The T and t variables chosen for the screening were substantially smaller than that used here to promote the significant formation of Tb_2Pc_3 (annealing temperature $T = 850$ K, annealing time $t = 60$ min). Furthermore, we compare how formation of Tb_2Pc_3 is driven at high annealing temperature at various times, after 60 min and 30 min of annealing in vacuum. Analysis of the mass spectra of the recovered material from the UHV crucible for the experiments performed at low temperatures and short times are given in detail in the ESI (Fig. S12,† annealing temperature 700 K, $t = 10$ min). Fig. S15 and S16† show the results obtained for the annealing temperature 850 K, and time $t = 30$ min experiment. In the low temperature and short annealing time scenarios, a barely detectable signature of the Tb_2Pc_3 specie is observed, together with barely detectable signals ascribable to decomposed/fragmented TbPc_2 molecules (range below $1000\ m/z^+$). Moreover, the mass spectra analysis for the material subjected to high temperature annealing under different annealing time indicates that formation of Tb_2Pc_3 is enhanced when longer times are employed (compare Fig. S9, $t = 60$ min to Fig. S16,† $t = 30$ min) and such process is accompanied by an increased presence of fragmented Pc ring/decomposed TbPc_2 molecules; thus, while the low-temperature experiments indicate that high annealing temperatures of the pristine TbPc_2 molecules inside the UHV chamber is a prerequisite for getting Tb_2Pc_3 formation, the annealing time is an equally important variable impacting the kinetics of the process, because it appears that longer times, together with high temperatures, favour both formation of substantial amounts of Tb_2Pc_3 but also substantial formation of TbPc molecules (half decker), as previously shown in the reaction

scheme depicted above (compare Fig. S9–S16 in the ESI,† where the absence of the TbPc peak at $703.1\ m/z^+$ can be noted in the latter).

Structural model

We performed detailed measurements and analysis of the arrangement of TbPc_2 and Tb_2Pc_3 assemblies on the Ag(111) surface. The nc-AFM technique provides unprecedented spatial resolution of molecular assemblies superior to standard STM imaging.⁴² In particular, the technique allows us to precisely measure the internal orientation of molecules forming the on-surface assembly.

Fig. 4 shows the multiple-height registration of the TbPc_2 relative to the Tb_2Pc_3 deduced from analysis of a single high-resolution AFM image of two domains of TbPc_2 and Tb_2Pc_3 molecules. We have directly measured the position and rotational orientation of the topmost Pc in both the double- and triple-decker species with respect to the Ag(111) lattice (more data shown in the ESI, Fig. S1 and S2†). We inferred the adsorption geometry of the bottom Pc ligand (black, Fig. 4c) from the atomic registration, and an equidistant ligand spacing due to steric repulsion, consistent with prior observations.⁴⁵ For the TbPc_2 molecules, we can directly add the topmost ligand from the experimental observations, with an alternating $30^\circ/45^\circ$ pattern relative to the bottom Pc (dark blue/red in Fig. 4b). For the Tb_2Pc_3 , we infer that the middle Pc conforms to the alternating $30^\circ/45^\circ$ pattern of the topmost TbPc_2 , and then add the topmost Pc, with a $\pm 5^\circ$ rotation relative to the bottom Pc (light blue/red).

From these observations, we can identify a two-molecule unit cell commensurate with the Ag(111) lattice (shown in ESI Fig. S2†). Unfortunately, such a big unit cell makes total energy DFT simulations computationally intractable. We per-

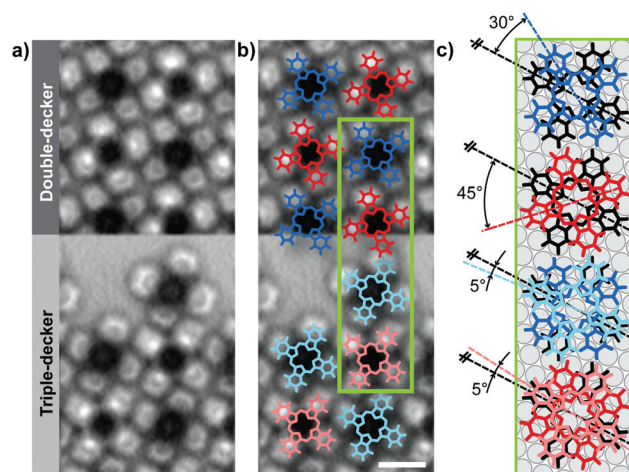


Fig. 4 nc-AFM registration of top Pc ligand and absorption model. (a) Multi-height nc-AFM resolving the top ligand of the TbPc_2 and Tb_2Pc_3 areas. (b) Orientation of the double-decker TbPc_2 and triple-decker Tb_2Pc_3 is shown with a superimposed model of the top Pc ligands. White scale bar is 1 nm. (c) Model showing the absorption sites of Pc on Ag(111) (black), and rotational orientations of the subsequent ligands.

formed calculations in a smaller unit cell including only one TbPc_2 or Tb_2Pc_3 species, respectively. This means that the mutual orientation cannot be directly compared to the experimental evidence. According to the total energy DFT simulations the TbPc_2 or Tb_2Pc_3 molecules are stabilised on the $\text{Ag}(111)$ surface by an attractive van der Waals interaction and charge transfer between the molecular species and metallic substrate. In both cases, we observed substantial planarization of the Pc ligands with respect to the optimal gas phase configuration (see inset in Fig. 2(c)), as a consequence of the attractive van der Waals interaction with the metallic substrate. The planar structure of the Pc ligands facilitates sub-molecular resolution measurements. Indeed, the calculated AFM images are consistent with the experimental data (see ESI Fig. S5†).

Molecular charge transfer

We extended the nc-AFM measurements to look for differences between the two observed rotational configurations, specifically a detailed examination of the charge distribution across molecule/surface interface and within each molecule. To analyze the charge transfer, we carried out Kelvin probe force microscopy (KPFM) measurements on the two species of molecules as well as the bare $\text{Ag}(111)$ (see ESI Fig. S4†). Differences in the capacitive term and local contact potential difference were observed between the three regions. We found the magnitudes of these parameters to be strongly dependent on the tip geometry and tip-sample distance, but the overall trend between Tb_2Pc_3 , TbPc_2 molecules and the Ag surface remained very similar. We observed differences in the contact potential difference V_{CPD} between the molecule regions and the bare $\text{Ag}(111)$, indicating that there is charge transfer occurring from the substrate towards the molecules, which is also accompanied by charge transfer between domains of Tb_2Pc_3 , TbPc_2 molecules. The charge transfer from the surface towards molecules is further supported by total energy DFT simulations of single TbPc_2 and Tb_2Pc_3 molecules deposited on $\text{Ag}(111)$ surface, as shown on Fig. 5. These models correspond to the 45° relative rotation, red molecules in Fig. 4(c). Namely, the DFT calculations indicates an extensive depletion of the electron density in surface area (see blue color iso densities shown on Fig. 5) under the molecule. On the other hand, we observe substantial charge redistribution in lower Pc and on Tb atom. This we attribute to molecular orbital reordering upon deposition on the $\text{Ag}(111)$ surface. Our simulations predict that upon surface deposition the eight f-electrons of Tb still remain lined up with a total spin $S = 3$ and a total orbital momentum $L = 3$. In the next section, we will show that the charge transfer plays an important role in the appearance of the Kondo effect.

Unfortunately, we do not observe differences on submolecular level between adjacent Tb_2Pc_3 molecules in the KPFM data. Nevertheless this level of spatial resolution for KPFM is likely limited by mesoscopic tip effects. In principle, we can improve it with an intentional CO-tip functionalization. But to obtain high spatial resolution, we have to operate the probe in close

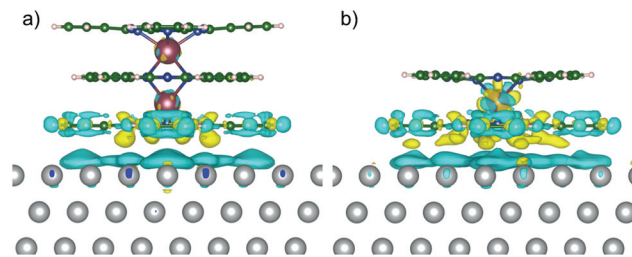


Fig. 5 Calculated charge transfer between Tb_2Pc_3 and TbPc_2 molecules (45° red molecules, Fig. 4c) and $\text{Ag}(111)$ surface obtained from DFT calculations. The charge transfer is represented by differential charge $\rho_{\text{ALL}} - \rho_{\text{mol}} - \rho_{\text{surf}}$, where ρ_{ALL} is total density of the whole system and ρ_{mol} and ρ_{surf} are calculated densities of molecule and $\text{Ag}(111)$ surface respectively. The yellow and blue colours represent accumulation and loss of density, respectively. The presence of blue density on the upper surface layer indicates substantial charge transfer from the metallic surface towards the molecule. The presence of both blue and yellow differential densities on the molecule reveals charge redistribution within the molecule upon charge transfer.

distances and large biases, which gives rise to spurious artefacts in the KPFM measurements.⁴⁶

Because of the limited spatial KPFM resolution we pursued a different approach to address differences in the internal charge distribution within molecules. Molecular backbones are typically represented by sharp edges caused by lateral bending of the CO-tip. Modification of the internal charge distribution within the molecule modifies the Coulombic interaction experienced by CO-tip. This in turn modifies the position of sharp edges providing information about the variation of the charge distribution.⁴⁷ We applied this methodology to this system to see if we could correlate the structural and electronic differences we observed in the sub-molecular AFM contrast. Fig. 6(a) and (b) are images of the same group of four Tb_2Pc_3 molecules, taken in standard STM with a metallic tip (Fig. 6a), and nc-AFM at constant height with a CO-functionalized probe (Fig. 6b). The top Pc ligand model is superimposed on Fig. 6(c) and (d) to guide the eye. The upper left- and right-hand molecules in Fig. 6(b) were imaged in greater detail, shown in Fig. 6(f) and (e) respectively. By filtering and registering these two images to one another, slightly different distortions in the benzene rings can be identified, as shown in Fig. 6(g). Namely, we observe a systematic elongation of benzene rings corresponding to red molecules (two lower Pc ligands are rotated by 45° with respect to each other, see Fig. 4c). Similar geometric distortions have been attributed to charge transfer effects, owing to the combination of Pauli repulsion, van der Waals and coulombic interaction of the CO-tip with the sample.^{47–50} Therefore, we attribute these differences in lateral distortion of benzene rings to different charge distributions in adjacent Tb_2Pc_3 molecules. Unfortunately, due to the lack of submolecular resolution of the internal part of the molecules, a direct comparison of the electrostatic potential between two Tb_2Pc_3 molecules with different internal orientations of Pc ligands cannot be accomplished.

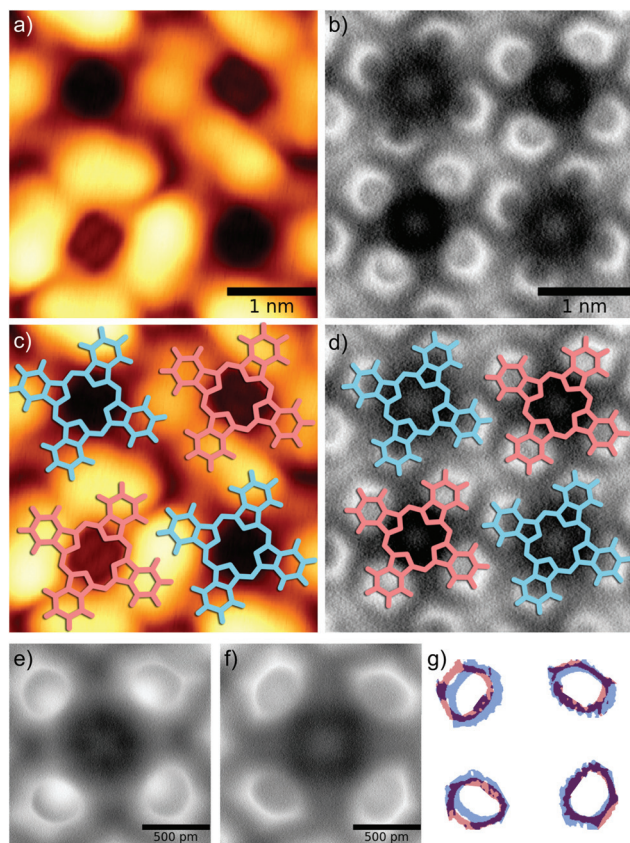


Fig. 6 Comparison of equivalent Tb_2Pc_3 regions with STM and nc-AFM imaging. (a) STM image measured on four molecules, $V_{\text{bias}} = 50$ mV, $I = 10$ pA. (b) nc-AFM image taken in constant height mode, recording the frequency shift in space over the same region as (a). (c) and (d) have the top PC ligand model overlaid to guide the eye. (e) and (f) are detailed images of the upper right- and left-hand molecules in (b), respectively. They are subsequently registered together and plotted in red (e)/blue (f) in (g).

It is noteworthy that very similar alternating distortions were also observed in adjacent TbPc_2 molecules with different internal rotations of Pc ligands. This indicates that the different rotations of lower and upper Pc ligands modifies the hybridization with the central Tb atoms and consequently modifies the charge distribution within the molecule.

Electronic structure of TbPc_2 and Tb_2Pc_3

Upon identifying the two distinct geometries of TbPc_2 or Tb_2Pc_3 in the surface assembly, we characterized their respective electronic properties. We carried out scanning tunneling spectroscopic (STS) measurements of the electronic structure, which show qualitative differences between distinctly orientated molecules of each species. Averaged STS spectra acquired on the ligand ring of two adjacent Tb_2Pc_3 and TbPc_2 molecules are plotted on Fig. 7(e) and (f), respectively. We clearly observe distinct positions of the highest occupied/lowest unoccupied molecular orbital (HOMO/LUMO) resonances for Tb_2Pc_3 and TbPc_2 molecules, which are spatially localized on the ligand. In the case of TbPc_2 molecules HOMO resonances are located

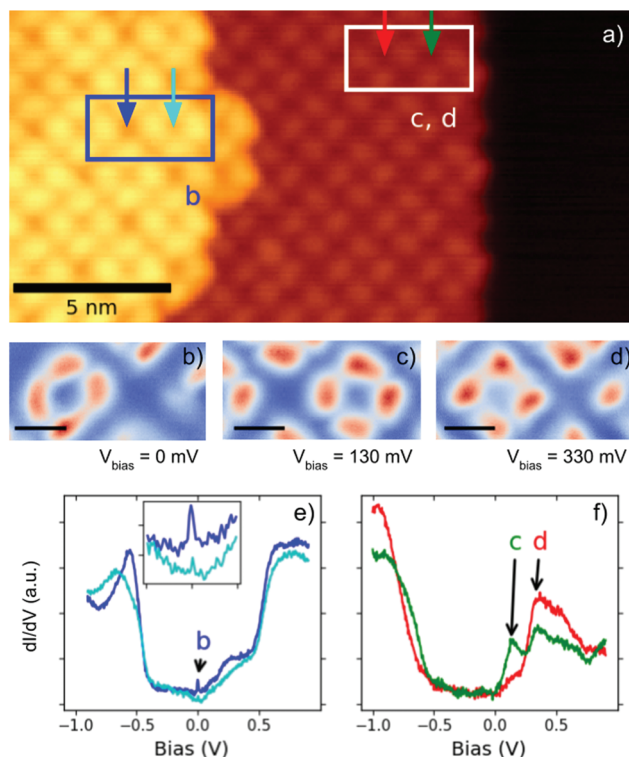


Fig. 7 Characterization of the electronic structure of Tb_2Pc_3 and TbPc_2 areas. (a) STM topography ($V_{\text{bias}} = 300$ mV, $I = 10$ pA) showing the locations for dI/dV spectroscopies averaged over the ligand (excluding the center) measured on adjacent molecules in the Tb_2Pc_3 (e) and TbPc_2 (f) layers. Constant height dI/dV mapping of the Kondo feature on the Tb_2Pc_3 layer ($V_{\text{bias}} = 0$) is shown in (b). Analogous maps of the TbPc_2 region at $V_{\text{bias}} = 130$ mV (c) and 330 mV (d). Scale bars for (b), (c), and (d) are 1 nm. Inset in (e) shows dI/dV for the bias range -0.1 to 0.1 V.

~ 0.2 eV lower in energy than those of Tb_2Pc_3 . We can also identify that the width of the HOMO peaks are directly linked to the internal rotation of Pc ligands, see Fig. 7(e). The lowest unoccupied states are spatially localized on Pc ligands similarly to the HOMO orbitals, as seen from spatial STS maps of two adjacent TbPc_2 with alternating relative Pc orientations at $V_{\text{bias}} = 130$ mV and 330 mV shown in Fig. 7(c) and (d), respectively.

The most significant observation from these data is the presence of the zero bias peak in the STS spectra only on one type of Tb_2Pc_3 molecule, while neither the second type of Tb_2Pc_3 nor TbPc_2 molecules display any evidence of the resonance. The alternating presence of the zero bias peak is also demonstrated explicitly in the real-space STS map at the Fermi level ($V_{\text{bias}} = 0$ V), shown in Fig. 7(b). The presence of the Kondo effect in TbPc_2 molecules deposited on different metal surface has already been reported by many groups.^{11,14,16,20,24,29–32,35,40} Consequently we attributed this zero bias peak to the Kondo resonance. Our spectroscopic measurements establish that the Kondo resonance appears only for the Tb_2Pc_3 molecules having the HOMO orbital located closest to the Fermi level. From the previous structural

analysis, we can assign the presence of the Kondo signature to the molecules overlaid with the light red model shown in Fig. 4(b), corresponding to the middle ligand having a 45° rotation relative to the bottom.

To estimate the Kondo temperature T_K of the Tb_2Pc_3 molecule showing the Kondo effect, we fit selected spectra using the Frota expression for the Kondo resonance:^{51,52}

$$\rho_F(\varepsilon) = \text{Im} \left[-i \sqrt{\frac{i\Gamma_F}{i\Gamma_F + \varepsilon}} \right], \quad (1)$$

with an additional linear background offset, where ε is the energy and Γ_F is proportional to the half width at half maximum. The Kondo temperature T_K can be calculated from Γ_F as follows:^{52,53} $\Gamma_F = 1.455k_B T_K$, where k_B is the Boltzmann constant. These fits indicate a temperature of approximately 30 K (± 5 K), consistent with prior measurements.²⁹ The Kondo temperature T_K has been averaged for several spectra acquired on different lobes of the upper Pc ligand, in positions indicated by red points in Fig. 8(b). There can be only one Kondo temperature for a given molecular state. We attribute the minor spatial variation of the Kondo resonance to experimental errors stemming from changes in the tip-sample distance due to thermal drift. We intentionally selected spectra in the central part of the ligand to minimise sensitivity to this error. The estimated Kondo temperature is far above the experimental temperature $T_{\text{exp}} = 5$ K, which indicates that the system is in the strongly coupled Kondo regime.

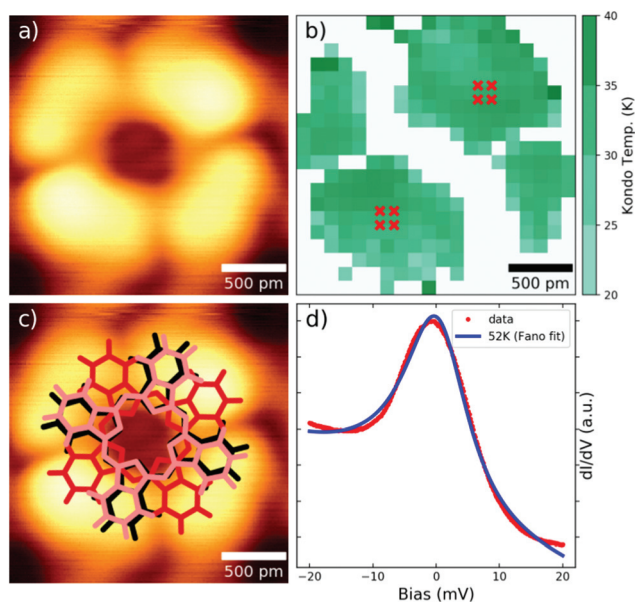


Fig. 8 Spatial mapping of the Kondo peak. (a) STM topography ($V_{\text{bias}} = 50$ mV, $I = 10$ pA) of the molecule subsequently mapped with grid spectroscopy. (b) Map of the fitted Kondo temperature on a single Tb_2Pc_3 species, showing a consistent temperature of approximately 30 K (Frota procedure) located on the Pc ligands. (c) Topography from (a) with Pc ligand superimposed to guide the eye. (d) Averaged point spectra showing the Kondo peak (x's on b; red points), and subsequently fit with the Fano procedure (blue).

Next, we analyze the Kondo effect in detail to gain further insight regarding its selective appearance on only the Tb_2Pc_3 molecules with the middle ligand rotated by 45° with respect to the bottom ligand. The presence of the Kondo resonance is intimately connected to the interaction of singly occupied magnetic impurity states with a bath of non magnetic electrons, typically located in a metallic substrate. This interaction leads to an effective screening of the spin of the localized state, which is manifested by presence of a sharp resonance in the spectral function at the Fermi level.⁵⁴ The width of the Kondo resonance Γ is proportional to the Kondo temperature T_K , which defines the relevant energy scale $k_B\Gamma$ of the Kondo effect. The Kondo temperature is determined by several factors, such as the position of the singly occupied state ε_i with respect to the Fermi level, its hybridisation with the substrate Δ and on-site Coulomb interaction U :⁵⁴

$$\Gamma = k_B T_K \approx \sqrt{2\Delta \frac{U}{\pi}} \exp \left[-\frac{\pi}{2\Delta} \left(\left| \frac{1}{\varepsilon_i} \right| + \left| \frac{1}{\varepsilon_i + U} \right| \right)^{-1} \right]. \quad (2)$$

Another parameter that plays an important role in the quantitative analysis of the Kondo problem is an average occupancy number n_i of the impurity state ε_i .⁵⁴ In our case, it is represented by the highest occupied molecular level. It has been demonstrated that the Kondo regime is typically established within an occupancy range of $0.8 < n_i < 1.2$ having approximately one unpaired electron in the highest occupied molecular level.⁵⁵ In the gas phase this is an integer number, but this is not necessarily the case upon deposition on a metallic surface due to additional interaction with the substrate. Indeed, we already established that both KPFM measurements and DFT calculations show charge transfer towards the molecule accompanied by additional charge transfer between domains of $TbPc_2$ and Tb_2Pc_3 . The high resolution AFM images reveal internal charge redistribution of the electrostatic field within molecules and the position of the HOMO with respect to the Fermi level induced by internal rotation of the Pc ligands.

We can estimate the occupancy n_i of the HOMO orbital of Tb_2Pc_3 molecules showing the Kondo resonance from analysis of the STS spectra using the well known Fano formula:⁵⁶

$$\rho(E) = \rho_0 + \frac{(q + \varepsilon)^2}{1 + \varepsilon^2}, \quad (3)$$

with an additional linear offset term, where ε is the normalized energy:

$$\varepsilon = \frac{E - E_K}{\Gamma_{\text{exp}}}. \quad (4)$$

E_K is the peak position, and Γ_{exp} is the half-width at half-maximum of the STS spectrum. q is the Fano parameter which interpolates between a Lorentzian peak ($q \rightarrow \infty$) and dip ($q = 0$), depending on the strength of the interference effect between competing tunneling channels through the single impurity and its environment. In our case, we obtained the best fit with parameters $E_K = 0.62$ meV, $\Gamma_{\text{exp}} = 6.3$ meV (blue

line, Fig. 8d). We correct the Γ width parameter for thermal broadening:⁵⁷

$$\Gamma = 2\sqrt{(\pi k_{\text{B}}T)^2 + 2(k_{\text{B}}T_{\text{K}})^2} \quad (5)$$

where we take $T = 5$ K as the temperature of the microscope (k_{B} is the Boltzmann constant). The corrected value $\Gamma = 4.3$ meV gives the Kondo temperature $T_{\text{K}} = 50$ K. This value is a little bit higher than the value obtained by the Frota fit. Finally, the occupation number n_i of the HOMO orbital can be deduced from the corrected Γ using the following expression:⁵⁴

$$E_{\text{K}} = \Gamma \tan\left(\frac{\pi}{2}(1 - n_i)\right). \quad (6)$$

We obtained the average occupation $n_i = 0.9$, which fits into the predicted range of occupancies where the Kondo effects may appear. We can check the consistency of this fit, by using the corrected value of $\Gamma = 4.3$ meV and solving eqn (2) subject to the additional constraint that $n_i = -\frac{\varepsilon_i}{U} + \frac{1}{2}$.⁵⁸ With this constraint, we obtained numerically optimised values for the Coulomb repulsion $U = 1.2$ eV; $\varepsilon_i = -480$ meV, the distance of the HOMO below the Fermi level; and $\Delta = 106$ meV, the width of the HOMO orbital. However, the excitation signal used for our measurements is large in comparison to the observed Kondo resonance, so these fit values have to be interpreted with considerable caution. That said, they reasonably match those from the experiment, which can be estimated from the STS spectra of the Tb_2Pc_3 molecule with Kondo resonance shown on Fig. 7(e): $U \sim 1.1$ eV, $\varepsilon_i \sim -550$ meV, and $\Delta \sim 150$ meV. In contrast, for the non-Kondo HOMO orbital (light blue, 7e) we estimate $\varepsilon_i \sim -650$ meV, and for TbPc_2 $\varepsilon_i \sim -950$ meV.

Based on the experimental evidence showing correlation between the position of HOMO orbitals with respect to the Fermi level and appearance of the Kondo resonance, we attribute the appearance of Kondo resonances to two factors: (i) the charge transfer from the surface to molecules and between different domains of TbPc_2 and Tb_2Pc_3 molecules, and (ii) the internal rotation of Pc ligands, further modifying the internal charge redistribution within molecules and importantly modifying the position of the highest occupied molecular resonance. Based on these observations, we propose the following scenario to rationalize the presence/absence of Kondo resonances in Tb_2Pc_3 and TbPc_2 molecules.

In the case of TbPc_2 molecules, it has been shown that the Kondo resonance observed on TbPc_2 molecules on Au(111) surface is related to the presence of an unpaired electron in the π -orbital of the upper Pc ligand, as discussed by Komeda *et al.*¹¹ However, in the case of the Ag(111) surface, the presence of a semi-occupied molecular orbital (SOMO) is suppressed by additional charge transfer upon deposition of the molecule on a metallic surface. This changes the occupancy of the HOMO and shifts its energy far from the Fermi level, and consequently the Kondo effect is quenched.

The situation is slightly different in the case of Tb_2Pc_3 molecules, where the three Pc^{2-} ligands accumulate a total

charge of -6 , which is fully compensated by charge $+6$ provided from the two Tb^{3+} . However, this neutrality is broken upon additional charge transfer towards the molecule after adsorption onto the surface, giving rise to the presence of an unpaired electron in the upper Pc ligand. In the case of the Tb_2Pc_3 , the presence of the Kondo resonance is further modulated by the internal rotation of the Pc ligand following the scenario proposed by Komeda *et al.*¹¹ Namely, the rotation of the Pc ligands changes the hybridization of the HOMO orbital, which shifts downwards its energy and increases its width. In principle, this effect increases the orbital occupancy of the HOMO level and reduces the effective exchange interaction between the localized electron in the HOMO and the bath of electrons. Consequently, the Kondo resonance disappears.

3. Conclusions

In summary, we have employed nc-AFM based techniques to identify our multiple height system as a mixture of TbPc_2 and Tb_2Pc_3 molecules, subsequently confirmed with separate chemical analysis. We established a structural model of the mixed Tb_2Pc_3 and TbPc_2 monolayer relative to the underlying Ag(111) surface using high-resolution AFM imaging. Spectroscopic measurements show the selective presence of a Kondo peak in the top ligand of alternating Tb_2Pc_3 species. High-resolution imaging of molecules exhibiting and lacking the Kondo peak show geometric distortions in the Pc ligand structure that we attribute to structural and charge environment differences. We use these structural measurements to model and simulate the charge transfer between the substrate in the various configurations: these quantitative differences are correlated with the qualitative appearance of the Kondo electronic signature. These data provide a comprehensive portrait for understanding the roles of structure and charge transfer in controlling the Kondo signature, and points to their utility in evaluating future candidate SMMs for use in surface based devices.

4. Methods

Experimental

Synthesis is accomplished by direct cyclization of the ring precursor (1,2-dicyanobenzene) at high temperatures in the presence of a metal salt (*e.g.* $\text{Tb}(\text{acac})_3$), 1,8-diazabicyclo(5.4.0)undec-7-ene (DBU) and high boiling solvents (*e.g.* pentanol, hexanol).^{9,59} The measurements described here were performed using commercial, ultrahigh vacuum (UHV) low-temperature microscopes with combined STM/nc-AFM capabilities (Specs-JT Kolibri: $f \sim 1$ MHz, $Q \sim 120\text{k}$, $K \sim 540$ kN m⁻¹, 50 pm amplitude and Createc-qPlus: $f_0 \sim 30$ kHz, $Q \sim 17\text{k}$, $K \sim 1.8$ kN m⁻¹, 50 pm amplitude). The Ag(111) single crystal (Mateck) was prepared by repeated Ar sputtering/annealing cycles. The TbPc_2 molecules were degassed in vacuum by repeated cycling to the evaporation temperature, 850 K. Coverages were obtained with a 15 min deposition in ambient pressure of 5×10^{-8} mbar (base pressure 1×10^{-10} mbar) with the Ag(111)

surface at 300 K (line-of-sight distance 30 cm), before subsequent insertion into the low-temperature microscope (5 K). CO was dosed onto the surface (pressure 8×10^{-8} mbar, 15 seconds) after the sample temperature was <10 K, for subsequent tip functionalization. STS point spectra and maps were acquired using the lock-in measurement technique, with an AC signal (~ 1 kHz) amplitude 5 mV (point/grid spectroscopies) or 15 mV (STS maps) added to the tip-sample junction. The presence of additional Tb_2Pc_3 molecules in the precursor TbPc_2 molecule batch that was annealed in UHV for the experiments was subsequently confirmed with matrix-assisted laser desorption/ionization (MALDI) spectroscopy (spectra shown in the ESI†).

Computational

The optimized structures of TbPc_2 and Tb_2Pc_3 molecules on Ag(111) were calculated by the FHI-AIMS program package⁶⁰ based on *ab initio* density functional theory (DFT). We used exchange correlation functional PBE + $U^{61,62}$ with $U = 5$ eV for f-electrons of Tb and van der Waals interaction was approximated by the Tkatchenko-Scheffler dispersion correction method.⁶³ The AFM images were calculated with Probe Particle code.^{48,64} We used the following parameters of the flexible probe-particle tip model: the effective lateral stiffness $k = 0.24$ N m^{-1} and effective atomic radius $R_c = 1.661$ Å. We added a quadrupole-like charge distribution at the tip apex to simulate the CO-tip for all the AFM simulations⁵⁰ (quadrupole charge of $-0.05 \times 0.71^2 e \text{ \AA}^2$).

Author contributions

P. J, M. S, J. H and A. C devised the experiments. J. H and A. C made the samples and did the measurements. B. T, T. C and M. M aided the UHV experiments. G. Z synthesized the molecules. G. Z and B. P performed the chemical analysis. P. M and P. J did the theoretical calculations. J. H, A. C, and P. J analyzed the data and composed the manuscript. All authors discussed the results and commented on the manuscript.

Conflicts of interest

There are no conflicts to declare.

Acknowledgements

The authors acknowledge insightful discussion with A. Schwarz regarding the interpretation of these data. This work was financially supported by the Czech Science Foundation (GACR) under Grants No. 14-374527G, 18-09914S, 17-24210Y, the Ministry of Education of the Czech Republic Grant LM2015087, Praemium Academiae program of the Academy of Science of the Czech Republic, and the SPP 1928 'COORNETS' of the German Science Foundation. The authors

gratefully acknowledge the support by the Operational Programme Research, Development and Education – European Regional Development Fund, project no. CZ02.1.01/0.0/0.0/16_019/0000754 of the Ministry of Education, Youth and Sports of the Czech Republic.

References

- 1 R. Sessoli, D. Gatteschi, A. Caneschi and M. A. Novak, *Nature*, 1993, **365**, 141–143.
- 2 D. Gatteschi, R. Sessoli and J. Villain, *Molecular Nanomagnets*, Oxford University Press, 2006.
- 3 D. N. Woodruff, R. E. P. Winpenny and R. A. Layfield, *Chem. Rev.*, 2013, **113**, 5110–5148.
- 4 E. Moreno Pineda, T. Komeda, K. Katoh, M. Yamashita and M. Ruben, *Dalton Trans.*, 2016, **45**, 18417–18433.
- 5 N. Ishikawa, S. Otsuka and Y. Kaizu, *Angew. Chem., Int. Ed.*, 2005, **44**, 731–733.
- 6 N. Ishikawa, Y. Mizuno, S. Takamatsu, T. Ishikawa and S. Y. Koshihara, *Inorg. Chem.*, 2008, **47**, 10217–10219.
- 7 N. Ishikawa, T. Iino and Y. Kaizu, *J. Am. Chem. Soc.*, 2002, **124**, 11440–11447.
- 8 K. Katoh, T. Kajiwara, M. Nakano, Y. Nakazawa, W. Wernsdorfer, N. Ishikawa, B. K. Breedlove and M. Yamashita, *Chem. – Eur. J.*, 2011, **17**, 117–122.
- 9 S. Stepanow, J. Honolka, P. Gambardella, L. Vitali, N. Abdurakhmanova, T.-C. C. Tseng, S. Rauschenbach, S. L. Tait, V. Sessi, S. Klyatskaya, M. Ruben and K. Kern, *J. Am. Chem. Soc.*, 2010, **132**, 11900–11901.
- 10 W. Kuch and M. Bernien, *J. Phys.: Condens. Matter*, 2017, **29**, 023001.
- 11 T. Komeda, H. Isshiki, J. Liu, Y.-F. Zhang, N. Lorente, K. Katoh, B. K. Breedlove and M. Yamashita, *Nat. Commun.*, 2011, **2**, 217.
- 12 A. Lodi Rizzini, C. Krull, T. Balashov, J. J. Kavich, A. Mugarza, P. S. Miedema, P. K. Thakur, V. Sessi, S. Klyatskaya, M. Ruben, S. Stepanow and P. Gambardella, *Phys. Rev. Lett.*, 2011, **107**, 177205.
- 13 R. Vincent, S. Klyatskaya, M. Ruben, W. Wernsdorfer and F. Balestro, *Nature*, 2012, **488**, 357–360.
- 14 J. Schwöbel, Y. Fu, J. Brede, A. Dilullo, G. Hoffmann, S. Klyatskaya, M. Ruben and R. Wiesendanger, *Nat. Commun.*, 2012, **3**, 953.
- 15 Y.-S. Fu, J. Schwöbel, S.-W. Hla, A. Dilullo, G. Hoffmann, S. Klyatskaya, M. Ruben and R. Wiesendanger, *Nano Lett.*, 2012, **12**, 3931–3935.
- 16 K. Katoh, H. Isshiki, T. Komeda and M. Yamashita, *Chem. – Asian J.*, 2012, **7**, 1154–1169.
- 17 A. Lodi Rizzini, C. Krull, T. Balashov, A. Mugarza, C. Nistor, F. Yakhov, V. Sessi, S. Klyatskaya, M. Ruben, S. Stepanow and P. Gambardella, *Nano Lett.*, 2012, **12**, 5703–5707.
- 18 R. Robles, N. Lorente, H. Isshiki, J. Liu, K. Katoh, B. K. Breedlove, M. Yamashita and T. Komeda, *Nano Lett.*, 2012, **12**, 3609–3612.

- 19 S. Thiele, F. Balestro, R. Ballou, S. Klyatskaya, M. Ruben and W. Wernsdorfer, *Science*, 2014, **344**, 1135–1138.
- 20 T. Komeda, K. Katoh and M. Yamashita, *Prog. Surf. Sci.*, 2014, **89**, 127–160.
- 21 S. Müllegger, S. Tebi, A. K. Das, W. Schöfberger, F. Faschinger and R. Koch, *Phys. Rev. Lett.*, 2014, **113**, 133001.
- 22 A. Lodi Rizzini, C. Krull, A. Mugarza, T. Balashov, C. Nistor, R. Piquerel, S. Klyatskaya, M. Ruben, P. M. Sheverdyeva, P. Moras, C. Carbone, C. Stamm, P. S. Miedema, P. K. Thakur, V. Sessi, M. Soares, F. Yakhou-Harris, J. C. Cezar, S. Stepanow and P. Gambardella, *Surf. Sci.*, 2014, **630**, 361–374.
- 23 M. Mannini, F. Bertani, C. Tudisco, L. Malavolti, L. Poggini, K. Misztal, D. Menozzi, A. Motta, E. Otero, P. Ohresser, P. Sainctavit, G. G. Condorelli, E. Dalcanale and R. Sessoli, *Nat. Commun.*, 2014, **5**(1), 4582.
- 24 T. Komeda, H. Isshiki, J. Liu, K. Katoh and M. Yamashita, *ACS Nano*, 2014, **8**, 4866–4875.
- 25 C. Nistor, C. Krull, A. Mugarza, S. Stepanow, C. Stamm, M. Soares, S. Klyatskaya, M. Ruben and P. Gambardella, *Phys. Rev. B: Condens. Matter Mater. Phys.*, 2015, **92**, 184402.
- 26 P. Robaschik, M. Fronk, M. Toader, S. Klyatskaya, F. Ganss, P. F. Siles, O. G. Schmidt, M. Albrecht, M. Hietschold, M. Ruben, D. R. T. Zahn and G. Salvan, *J. Mater. Chem. C*, 2015, **3**, 8039–8049.
- 27 Y. Zhang, P. Liao, J. Kan, C. Yin, N. Li, J. Liu, Q. Chen, Y. Wang, W. Chen, G. Q. Xu, J. Jiang, R. Berndt and K. Wu, *Phys. Chem. Chem. Phys.*, 2015, **17**, 27019–27026.
- 28 M. Perfetti, M. Serri, L. Poggini, M. Mannini, D. Rovai, P. Sainctavit, S. Heutz and R. Sessoli, *Adv. Mater.*, 2016, **28**, 6946–6951.
- 29 F. Ara, Z. K. Qi, J. Hou, T. Komeda, K. Katoh and M. Yamashita, *Dalton Trans.*, 2016, **45**, 16644–16652.
- 30 K. Katoh, T. Komeda and M. Yamashita, *Chem. Rec.*, 2016, **16**, 987–1016.
- 31 B. Warner, F. El Hallak, N. Atodiresei, P. Seibt, H. Prüser, V. Caciuc, M. Waters, A. J. Fisher, S. Blügel, J. van Slageren and C. F. Hirjibehedin, *Nat. Commun.*, 2016, **7**, 12785.
- 32 G. Serrano, S. Wiespointner-Baumgarthuber, S. Tebi, S. Klyatskaya, M. Ruben, R. Koch and S. Müllegger, *J. Phys. Chem. C*, 2016, **120**, 13581–13586.
- 33 C. Wäckerlin, F. Donati, A. Singha, R. Baltic, S. Rusponi, K. Diller, F. Patthey, M. Pivetta, Y. Lan, S. Klyatskaya, M. Ruben, H. Brune and J. Dreiser, *Adv. Mater.*, 2016, **28**, 5195–5199.
- 34 S. Marocchi, A. Candini, D. Klar, W. Van den Heuvel, H. Huang, F. Troiani, V. Corradini, R. Biagi, V. De Renzi, S. Klyatskaya, K. Kummer, N. B. Brookes, M. Ruben, H. Wende, U. del Pennino, A. Soncini, M. Affronte and V. Bellini, *ACS Nano*, 2016, **10**(10), 9353–9360.
- 35 A. Amokrane, S. Klyatskaya, M. Boero, M. Ruben and J.-P. Bucher, *ACS Nano*, 2017, **11**, 10750–10760.
- 36 M. Serri, M. Mannini, L. Poggini, E. Vélez-Fort, B. Cortigiani, P. Sainctavit, D. Rovai, A. Caneschi and R. Sessoli, *Nano Lett.*, 2017, **17**, 1899–1905.
- 37 M. Urdampilleta, S. Klyatskaya, M. Ruben and W. Wernsdorfer, *ACS Nano*, 2015, **9**, 4458–4464.
- 38 C. Godfrin, A. Ferhat, R. Ballou, S. Klyatskaya, M. Ruben, W. Wernsdorfer and F. Balestro, *Phys. Rev. Lett.*, 2017, **119**, 1–5.
- 39 E. Moreno-Pineda, C. Godfrin, F. Balestro, W. Wernsdorfer and M. Ruben, *Chem. Soc. Rev.*, 2017, **47**, 501–513.
- 40 K. Katoh, Y. Yoshida, M. Yamashita, H. Miyasaka, B. K. Breedlove, T. Kajiwara, S. Takaishi, N. Ishikawa, H. Isshiki, F. Z. Yan, T. Komeda, M. Yamagishi and J. Takeya, *J. Am. Chem. Soc.*, 2009, **131**, 9967–9976.
- 41 L. Vitali, S. Fabris, A. M. Conte, S. Brink, M. Ruben, S. Baroni and K. Kern, *Nano Lett.*, 2008, **8**, 3364–3368.
- 42 P. Jelínek, *J. Phys.: Condens. Matter*, 2017, **29**, 343002.
- 43 B. Schuler, W. Liu, A. Tkatchenko, N. Moll, G. Meyer, A. Mistry, D. Fox and L. Gross, *Phys. Rev. Lett.*, 2013, **111**, 106103.
- 44 N. Moll, L. Gross, F. Mohn, A. Curioni and G. Meyer, *New J. Phys.*, 2010, **12**, 125020.
- 45 Y. Bai, F. Buchner, M. T. Wendahl, I. Kellner, A. Bayer, H.-P. Steinrück, H. Marbach and J. M. Gottfried, *J. Phys. Chem. C*, 2008, **112**, 6087–6092.
- 46 F. Albrecht, J. Repp, M. Fleischmann, M. Scheer, M. Ondráček and P. Jelínek, *Phys. Rev. Lett.*, 2015, **115**, 076101.
- 47 P. Hapala, M. Švec, O. Stetsovych, N. J. van der Heijden, M. Ondráček, J. van der Lit, P. Mutombo, I. Swart and P. Jelínek, *Nat. Commun.*, 2016, **7**, 11560.
- 48 P. Hapala, R. Temirov, F. S. Tautz and P. Jelínek, *Phys. Rev. Lett.*, 2014, **113**, 226101.
- 49 B. de la Torre, M. Švec, G. Foti, O. Krejčí, P. Hapala, A. Garcia-Lekue, T. Frederiksen, R. Zbořil, A. Arnau, H. Vázquez and P. Jelínek, *Phys. Rev. Lett.*, 2017, **119**, 166001.
- 50 J. Peng, J. Guo, P. Hapala, D. Cao, R. Ma, B. Cheng, L. Xu, M. Ondráček, P. Jelínek, E. Wang and Y. Jiang, *Nat. Commun.*, 2018, **9**, 122.
- 51 H. O. Frota, *Phys. Rev. B: Condens. Matter Mater. Phys.*, 1992, **45**, 1096–1099.
- 52 H. Prüser, M. Wenderoth, P. E. Dargel, A. Weismann, R. Peters, T. Pruschke and R. G. Ulbrich, *Nat. Phys.*, 2011, **7**, 203–206.
- 53 R. Žitko and T. Pruschke, *Phys. Rev. B: Condens. Matter Mater. Phys.*, 2009, **79**, 1–17.
- 54 A. C. Hewson, *The Kondo Problem to Heavy Fermions*, Cambridge University Press, Cambridge, UK, 1993.
- 55 V. Zlatić, B. Horvatić and D. Šokčević, *Z. Phys. B: Condens. Matter*, 1985, **59**, 151–157.
- 56 U. Fano, *Phys. Rev.*, 1961, **124**, 1866–1878.
- 57 K. Nagaoka, T. Jamneala, M. Grobis and M. F. Crommie, *Phys. Rev. Lett.*, 2002, **88**, 4.
- 58 O. Újsághy, J. Kroha, L. Szunyogh and A. Zawadowski, *Phys. Rev. Lett.*, 2000, **85**, 2557–2560.

- 59 F. Branzoli, P. Carretta, M. Filibian, G. Zoppellaro, M. J. Graf, J. R. Galan-Mascaros, O. Fuhr, S. Brink and M. Ruben, *J. Am. Chem. Soc.*, 2009, **131**, 4387–4396.
- 60 V. Blum, R. Gehrke, F. Hanke, P. Havu, V. Havu, X. Ren, K. Reuter and M. Scheffler, *Comput. Phys. Commun.*, 2009, **180**, 2175–2196.
- 61 J. P. Perdew, K. Burke and M. Ernzerhof, *Phys. Rev. Lett.*, 1996, **77**, 3865–3868.
- 62 S. L. Dudarev, G. A. Botton, S. Y. Savrasov, C. J. Humphreys and A. P. Sutton, *Phys. Rev. B: Condens. Matter Mater. Phys.*, 1998, **57**, 1505–1509.
- 63 A. Tkatchenko and M. Scheffler, *Phys. Rev. Lett.*, 2009, **102**, 073005.
- 64 P. Hapala, G. Kichin, C. Wagner, F. S. Tautz, R. Temirov and P. Jelínek, *Phys. Rev. B: Condens. Matter Mater. Phys.*, 2014, **90**, 085421.